LAWRENCE
LIVERMORE
NATIONAL
LABORATORY

UCRL-JRNL-218431

Orientation relationship, plasticity, twin relationship, and interfacial structure of the ???' isothermal martensitic transformation in Pu-Ga alloys

K. Moore, C. Krenn, M. Wall, A. Schwartz

January 26, 2006

Metallurgical and materials transactions

Orientation relationship, habit plane, twin relationship, interfacial structure, and plastic deformation resulting from the δ→α' isothermal martensitic transformation in Pu-Ga alloys

Kevin T. Moore, Chris R. Krenn, Mark A. Wall, and Adam J. Schwartz
Lawrence Livermore National Laboratory, Livermore, CA 94550, USA.

Abstract: The orientation relationship, habit plane, parent-product interface at the atomic level, twin relationship, and plastic deformation resulting from the δ→α' isothermal martensitic transformation in Pu-Ga alloys are examined using optical microscopy, transmission electron microscopy, and finite element calculations. The δ→α' transformation exhibits a ~20% volume collapse when the face-centered cubic δ phase transforms to the monoclinic α′ phase, which results in unique and intriguing crystallography and morphology. Here, we show that the orientation relationship is very close to that previously reported by Zocco *et al.* (1990), but has small rotational misalignments between the two phases both parallel and perpendicular to the $[110]_{\delta} \,||\, [100]_{\alpha'}$ direction. The amount of plastic deformation is exceedingly large due to the ~20% volume collapse and transmission electron microscopy is used to quantify the difference in dislocation density between untransformed δ-matrix and regions of δ adjacent to the transformed α'. The twins contained in α' plates are shown to have a $(205)_{\alpha}$ orientation as the lattice invariant deformation and are found to be composed of two alternating variants that share a common $<020>_{\alpha'}$ direction, but differ by a 60 degree rotation about $<020>_{\alpha'}$. A combination of electron diffraction and optical microscopy has been employed to examine the macroscopic habit plane and the analysis suggests that a large fraction of the observed habit planes are on or near $\{111\}_{\delta}$. Finally, high resolution transmission electron microscopy reveals that the interface is faceted on $\{111\}_{\delta}$, exhibiting a series of terrace and ledges.

Keywords: plutonium, transmission electron microscopy, habit plane, phase transformation

§1. INTRODUCTION

Plutonium is a fascinating metal that exhibits a wide range of strange behaviors [1]. Most all of these behaviors emanate from the complicated electronic structure, which is dominated by the 5*f* states. While the δ→α' phase transformation is the primary topic of this paper, we will address the electronic structure in the introduction, since it is so integrally tied to the behavior of plutonium. In doing so, we hope to continue to merge the physics understanding of the electronic structure with the materials science understanding of the phase transformation and phase stability.

The bonding of the 5*f* metals along the actinide series can be separated into two different behaviors, one where the 5*f* electrons participate in bonding and one where they do not. This can be seen in Figure 1, where the Wigner-Seitz atomic radius (volume) is given for each element in the 5*d*, 4*f*, and 5*f* metal series [2]. The 5*d* transition metals show a parabolic change in volume due to an increase in the number of electrons. In traversing the 5*d* series, the size of the atoms first decreases due to the filling of the 5*d* bonding states, then begins to increase as the antibonding states are filled. This parabolic behavior is indicative of a system with itinerant (i.e., bonding) electrons. In the 4*f* rare earth series, the volume changes very little because the 4*f* electrons do not participate in bonding. Rather, only the $(spd)^3$ electrons act to bind the metals, and because the *spd* electrons do not vary in count along the rare earth series there is little change in packing density. Finally, the 5*f* series first shows a parabolic decrease in volume similar to the 5d series with increasing *f*-electron count, then a large jump in radius in the vicinity of Pu,

followed by little change in radius for Am and beyond. In the 5*f* states, the 5/2 and 7/2 sublevels are well separated due to the large 2 eV spin-orbit splitting that occurs in the states [3,4]. Therefore, the first part of the series shows a parabolic shape due to the filling of the bonding and antibonding states in the 5/2 sublevel [5]. Then, near Pu the 5*f* electrons retract and decrease bonding in the metal, leaving the $(spd)^3$ electrons to perform the bulk of the bonding. This reduction of the 5*f* bonding causes a large volume increase, which can be seen in Figure 1 [2]. This change occurs over the span of the 6 solid allotropic phases (α,β,γ,δ,δ′,ε: see table 1) of Pu, where α has the highest density and δ the lowest, even though it exhibits the close-packed fcc structure. Finally, the end of the series appears similar to the rare earths due to the absence of *f* electrons strongly participating in the bonding of the metal.

The changes that occur in the actinide series as Pu is approached can be better visualized in the 'pseudo-phase' diagram as shown in Figure 2 [6]. Here it can be seen that i) the melting temperature reduces and reaches a minimum at Pu, ii) the number of phases increases and reaches a maximum at Pu, and iii) the complexity of the phases increases with increasing number of *5f* electrons approaching Pu. This diagram also illustrates the intriguing behavior does not just occur at Pu, but is present in the light actinides and comes to a zenith at plutonium.

The unique behaviors of Pu illustrated above can be further understood by examination of the rearranged periodic table in Figure 3(a), which shows the five transition metal series; 4*f*, 5*f*, and 3*d* to 5*d* [6,7]. At ground state, the metals in the blue area exhibit

superconductivity and the metals in the red area exhibit a magnetic moment. The white band is a transition region where metals are on the borderline between localized (magnetic) to itinerant (conductive) valence electron behavior. Notice that Pu falls on this transition along with Mn, Fe, and Ce, each of which is considered a complex metal in relation to aluminum.

These metals at the transition between magnetic and superconductive behavior exhibit crystallographic phase instability. Figure 3(a) can be extended to reveal this instability of the metals that lie on the itinerant-localized transition by assigning a gray scale to the number of solid allotropic phases observed [8]. In Figure 3(b), the instability along the transition becomes evident by the diagonal of lighter shades that matches the white band in Figure 3(a). Of all the metals that lie on the transition and exhibit multiple solid allotropic phases, Pu is the most enigmatic with 6. Each of these 6 phases is very close in energy [9], thus transformation from one phase to another is easily achieved via pressure, temperature, and chemistry and often limited simply by kinetics. Certainly this small difference in the energy between the solid allotropic phases influences the phase transformations observed in Pu and its alloys.

Turning our attention to pure Pu and its alloys, the atomic volume as a function of temperature is shown in Figure 4 [2]. Here, the large number of phases can be seen, as well as the significant volume differences between each phase. The symmetry of the structures ranges from monoclinic in the α phase to face-centered cubic in the δ phase (see table 1). Also of interest is the negative coefficient of thermal expansion seen in

both δ and δ′ and the fact that both the ε phase and the liquid phase are more dense than δ and δ′.

When Pu is alloyed with a few percent of trivalent metals such as Al, Ga, Ce, or Am, the readily machinable fcc δ phase can be retained in a metastable state at room temperature [1]. The Pu-rich side of the Pu-Ga binary phase diagram is shown in Figure 5 [10]. While the thermodynamically stable phase diagram shows δ-Pu separating into α + Pu_3Ga at room temperature, kinetics limits the transformation such that δ-Pu is stable for thousand of years, even with self-radiation damage [10]. However, when the metastable Ga-stabilized fcc Pu is cooled to below -120°C an isothermal martensitic transformation to the monoclinic α′-phase occurs. A time-temperature-transformation (TTT) diagram for a Pu - 0.56 wt% Ga alloy, as shown in Figure 6, illustrates how the transformation to α′ proceeds with time at a given temperature [11]. Notice that there are two noses on the TTT curve, one at -130°C and one at -155°C, suggesting that there are two distinct thermally activated mechanisms existing for this transformation. A maximum of about 25% transformation to α′ occurs, beyond which little additional transformation is observed. This is most likely due to the large amount of plastic deformation and internal stress that must be produced during the ~20% volume reduction that occurs in the δ→α′ martensitic transformation. It should be noted that a TTT diagram with two noses is rather uncommon and that this adds yet another intriguing piece to the Pu puzzle.

The transformation between δ and α′ also exhibits a large hysteresis that is evident in the continuous cooling dilatometry trace shown in Figure 7 [12]. A simple thermodynamic

explanation for this is due to the large amount of plastic work associated with the transformation [13-15]. We can write the free energy change of the δ→α′ transformation as a sum of four terms:

$$\Delta G_{\delta \to \alpha'} = \Delta G_{\delta \to \alpha'}^{chem} + \Delta G_{\delta \to \alpha'}^{elastic} + \Delta G_{\delta \to \alpha'}^{plastic} + \Delta G_{\delta \to \alpha'}^{surface}, \quad (1)$$

where $\Delta G_{\delta \to \alpha'}^{chem}$ is the free energy change during the formation of unconstrained α′, $\Delta G_{\delta \to \alpha'}^{elastic}$ is the elastic energy arising from the lattice parameter mismatch, and $\Delta G_{\delta \to \alpha'}^{surface}$ is the surface energy for the creation of δ/α′ interfacial area. $\Delta G_{\alpha \to \beta}^{plastic}$ is not strictly speaking a "free energy", but it represents the energy required to create and move dislocations as well as the heat dissipated during the plastic accommodation process. Additional undercooling is required below the stress-free thermodynamic equilibrium transformation temperature, where $\Delta G_{\delta \to \alpha'}^{chem} = 0$, to provide sufficient driving force to overcome the other terms in Eqn. 1, which are all positive. The free energy change during the reverse transformation has the same form:

$$\Delta G_{\alpha' \to \delta} = \Delta G_{\alpha' \to \delta}^{chem} + \Delta G_{\alpha' \to \delta}^{elastic} + \Delta G_{\alpha' \to \delta}^{plastic} + \Delta G_{\alpha' \to \delta}^{surface}, \quad (2)$$

but the values of the elastic and surface energy terms are approximately equal and opposite to the corresponding terms in Eqn. 1. However, because the vast majority of plastic work is dissipated as heat, the sign of the plastic term is still positive. When the amounts of plastic deformation are large, as they are in the case of the δ→α′ phase transformation in plutonium, significant superheating above the unconstrained transformation temperature is required to reverse the transformation. Since the elastic work and changes in surface energy during the forward and reverse transformations are

roughly equal and opposite [14,15], the width of the hysteresis is proportional to the sum of the forward and reverse plastic works of transformation. We shall show that the large volume reduction that occurs in the δ→α′ martensitic transformation results in significant plastic strain fields, and these can be visualized through both experiments and calculations.

This introduction has illustrated the highly unique behavior of plutonium metal and its alloys compared to most other metals in the Periodic Table. Here, we will focus on the δ→α′ martensitic transformation that occurs in Pu-Ga alloys at low temperatures, including the α′ habit plane, α′/δ orientation relationship, parent-product interface at the atomic level, twin relationship, and plastic deformation resulting from the transformation. The information in this introduction will be repeatedly referred to in the following sections and used as a general knowledge-base with which to help better understand the entire picture of the δ→α′ martensitic transformation.

§2. MATERIALS AND METHODS

We investigated a Pu-0.6 wt% Ga alloy using optical microscopy and transmission electron microscopy (TEM). The alloy was prepared by induction heating and was approximately two years old. After casting, preannealing, and rolling, the material was annealed for at 425-440°C to partially homogenize the Ga distribution. The δ→α′ transformation was induced by quenching to either -120°C or –155°C, which were in the upper and lower "c-curves," respectively (see figure 6). Specimens for optical

microscopy were mechanically polished and then lightly etched chemically. Samples were prepared for TEM by electropolishing 3mm diameter discs, 150μm thick, to electron transparency using a Fischione Instruments electropolishing system using a solution of 10% nitric acid (70% concentration), 45% methanol, and 45% butoxyethanol (butylcellusove) by volume. The parameters for electropolishing were as follows: 20°C, 35 V and 40 mA. The specimen was thinned continuously to perforation. After perforation, the sample is immediately re-polished at a higher voltage (50 V) for 2–3 s to remove a thin anodic film that develops during the continuous polishing at lower voltages. The thinning process was performed in an inert atmosphere glove box and the samples were transferred under vacuum to the TEM using a vacuum-transfer specimen holder [16].

Imaging and diffraction experiments were performed using a Philips CM300 field-emission-gun TEM operating at 297 kV. Zero-loss filtered images and diffraction patterns were digitally acquired using a Gatan imaging filter with a charge-coupled-device camera with a 2048 pixels x 2048 pixels array. Zero-loss filtering removes inelastic electron scatter, leaving intensity due only to elastic scatter. This yields images and diffraction patterns that are sharper and reveal more details.

§3. RESULTS

3.1. *Orientation relationship*

The α′/δ orientation relationship observed in the present work is the same as previously reported by Zocco *et al.* [17]:

$$(111)_{\delta} \,||\, (020)_{\alpha'}$$
$$[110]_{\delta} \,||\, [100]_{\alpha'}$$

A two-phase mixture of α′ and δ that was formed by cooling a Pu-Ga sample to -120°C for 10 hours is shown in Figure 8 (a). The α′ plate is easily seen due to the strong mass contrast caused by the 20% volume difference between α′ and δ. While the α′/δ interface is not rigidly parallel to any given plane there is certainly not a tendency for a large degree of curvature. A diffraction pattern of a two-phase mixture is shown in Figure 8 (b), with the reflections for α′ and δ labeled. An atomic model is presented in Figure 8 (c) that schematically shows the orientation relationship of α′ and δ at the atomic level. Here, the atomic interface is assumed to be planar along $(111)_{\delta} \,||\, (020)_{\alpha'}$; however, we will later show the interface is more complex with a series of ledges and terraces.

While the above orientation relationship is close to exact, there is always some degree of misalignment between α′ and δ in the two-phase diffraction patterns. Along the $[110]_{\delta} \,||\, [100]_{\alpha'}$ direction either the $[110]_{\delta}$ or $[100]_{\alpha'}$ zone axis can be aligned parallel to

the electron beam, but the other axis is always a fraction of a degree misaligned and +**g** and –**g** are not of even intensity. This means that while the $[110]_{\delta}$ and $[100]_{\alpha'}$ directions are close to parallel, they are not exactly parallel. In addition, there is in-plane rotation observed in the two-phase $[110]_{\delta} \,||\, [100]_{\alpha'}$ diffraction patterns. Using the 111_{δ} and $020_{\alpha'}$ reflections as markers, a rotation between 0.5 and 1.5° is consistently observed about the $[110]_{\delta} \,||\, [100]_{\alpha'}$ direction. Thus, we again see that the above orientation relationship is close, but not exact.

The variation in rotation observed parallel and perpendicular to $[110]_{\delta} \,||\, [100]_{\alpha'}$ (in and out of the diffraction plane) may be caused by variations in the strain within the lattice or composition variations (giving rise to variations in lattice parameter) within the δ matrix. The amount of plastic deformation varies in different areas of the partially transformed δ + α′ Pu-Ga two-phase mixture, meaning that the strain is not uniform in the matrix. The dislocation density within the matrix, which is addressed in the next section, may even cause slight rotation changes between the two phases from one part of an α′ plate to another.

3.2. *Plastic deformation resulting from the transformation*

The volume reduction that occurs in the δ→α′ martensitic transformation is approximately 20%, so the amount of plastic deformation that occurs during transformation is accordingly large. In order to better understand this, we have performed both calculations and transmission electron microscopy. Elastic-plastic finite

element calculations can be used to visualize the stress induced by the δ→α′ martensitic transformation, and this is shown in Figure 9(a) [14]. Here, the compressive and tensile stresses are shown for a fcc matrix that has first grown an α′ plate, then reverted back to fcc δ-phase. The large and isolated strain fields near the tip of the α′ plate are evident in Figure 9(a). Examining a two-phase Pu-Ga alloy using transmission electron microscopy (Figure 9 b and c), we find the average dislocation density near the α′ plates is 1.7 x $10^{11}/cm^2$, while the average density away from the plates (~ 5-7 μm) in the same sample is 2.2 x $10^{10}/cm^2$. Thus, the dislocation density is 7.7 times higher in the vicinity of the α′ plates compared to the distant matrix in transformed samples. The average dislocation density in this same material after being annealed at 300°C for 4 hours is 1.97 x $10^9/cm^2$; a reduction in dislocation density of 86 times compared to the highly-damaged regions near the α′ plates and by 11 times compared to the distant matrix.

The large volume change and resulting increase in dislocation density during the transformation causes the incomplete transformation of δ to α′ observed in Figure 6 and the large hysteresis observed in Figure 7. Upon transformation when cooling, isolated plates can form with a sufficient amount of undercooling. However, when the plates start to interact, the elastic and plastic terms in Eqn. 1 become larger and larger until the transformation arrests itself after only 20 – 25% transformation. When the system is then heated, the α′ plates are not reverted until the system is well above ~70 °C, due to the need to overcome the significant plastic work of the transformation. We note that without plastic deformation, the elastic energies would be much higher, and the original δ to α′ transformation would be impossible.

One question of interest is whether the α′ plates retain crystallographic registry with the surrounding matrix when they revert back to delta upon heating, or whether new delta crystals are nucleated. In the latter case, a plate-shaped single crystal of δ could remain where the α′ plate was and have an orientation different from the matrix, or it could be composed of numerous small grains of delta. In order to investigate this, we are planning a number of hot-stage experiments using both optical and transmission electron microscopy. Past experiments and analyses [18] have strongly suggested that the plates do indeed keep crystallographic registry and no new delta grains are formed. If in fact new crystals were formed, dilatometry and resistivity measurements during repetitive thermal cycling would change. When Pu-Ga samples are repeatedly cycled without annealing, the cycles do become increasing displaced [19]. However, when the samples are annealed after a low-temperature experiment, then conditioned at room temperature for at least 6 hours, they exhibit the same traces upon multiple runs [20]. For small grains to be consumed by larger ones and to have appreciable grain growth occur, considerable annealing must take place at high temperature and for long periods. However, experiments show that this type of anneal is not needed to ensure the low-temperature experiment exhibit the same traces upon multiple runs. Thus, the change (compression) of the dilatometry trace upon cycling is likely due to the accumulation of damage in the lattice and not the production of new δ grains where the α′ plates had been.

3.3. *Twin relationship in α′*

Transmission electron microcopy reveals that the α′ plates usually contain numerous twins, as shown in the TEM image of an α′ plate contained in a δ matrix in Figure 10 (and Figure 8). The twins have a $(205)_{\alpha}$ orientation as the lattice invariant deformation mode, as previously observed by Zocco *et al.* [17]. The α′ plates are composed of two alternating twin variants that share a common $<020>_{\alpha'}$ direction, but differ by a 60 degree rotation about $<020>_{\alpha'}$. This can be seen in the images of Figure 10, where the corresponding diffraction pattern shows the reflections of the two variants used for the dark-field TEM images. Examination of the dark-field images in Figure 10 reveals the alternating twin slabs in the α′ plate.

The twin structure of the α′ plates is illustrated with the model presented in Figure 11. Again the $<020>_{\alpha'}$ direction is shared by both variants, but a 60 degree rotation about that axis is imposed. This produces Variant #1 and Variant #2, which generate the diffraction patterns shown in the upper-right side of the Figure. When these two diffraction patterns are superimposed with the diffraction pattern of the δ matrix, which due to the orientation relationship is near a $\{110\}_{\delta}$-type orientation, the result is the calculated selected-area diffraction pattern shown in the lower-left side of Figure 11. When compared to an experimental diffraction pattern that contains both the δ matrix and both α′ twin variants, a very good match is achieved. Because the structure of α′ can be viewed as a distorted hcp structure [21] with quasi-close-packed dimensions of 3.00 Å, 3.09 Å and 3.21 Å, it is reasonable that alternation of two or three variants will minimize the α′/δ interfacial

energy. The reason that only two variants are observed could be attributed to more subtle details of the twin interfacial energies or to geometric constraints of the martensitic growth.

The calculations of Jin *et al.* [22] showed that the $(205)_\alpha$ twin is the energetically-preferred twin (for their variants 1 and 4). While these calculations do not show that the twist minimizes the invariant plane strain, it probably does minimize interface energy. Thus, we conclude full agreement between theory and experiment that the $(205)_\alpha$ twin is the lattice invariant deformation mode.

3.4. *Macroscopic habit plane of α′ plates*

The macroscopic habit plane of α′ plates was shown to be near $\{123\}_\delta$ via both theory [23] and experiment [17]. Assuming a habit plane of $\{123\}_\delta$, 24 variants of α′ are produced in the fcc matrix due to symmetry operations. Our experiments have repeatedly revealed not 24, but rather ~4 variants. As an example, an elastic phase-field simulation of the growth and intersection of α′ plates in a single crystal of δ is shown in Figure 12 [14]. Here, there are 24 variants as would be expected from $\{123\}_\delta$ habit plane. However, the optical micrograph in Figure 12 shows many fewer variants, and in fact looks very much like plates on a {111} habit plane when looking parallel to a <110> direction of an fcc crystal. Because of this discrepancy between previous experiment and theory and our present experiments, we have considered that the current crystallographic

model of α′ is inconsistent, thus motivating further microstructural examination of the macroscopic habit plane of α′ in the δ→α′ martensitic transformation.

The determination of the macroscopic habit plane(s) of the α′ plates has been quite difficult due to numerous reasons. First, there are large variations in the system due to the fact that Pu is highly sensitive to processing, making it intrinsically a difficult system to study. In addition, Pu very rapidly oxidizes, it is radioactive, and we are able to characterize only a limited number of samples per year. The high *Z* number and large thermal diffuse scattering make TEM difficult, and we have no access to electron backscatter diffraction, making crystallographic orientation determination on bulk samples difficult. To date, and given the above problems, we have found our best solution to be the combination of TEM and optical imaging. We will discuss this in length, but first we will discuss analysis of only optical images of two-phase material containing α′ and δ.

An optical image of a two-phase mixture of α′ and δ is shown in Figure 13 [14,17]. The α′ plates are easily seen in the micrograph as white plates in the dark δ matrix. There are also three separate grains of δ, each delineated by black lines. The α′ plates are clearly adopting a well-defined macroscopic habit plane as evidenced by the large sets of plates grouped into the same configuration. The next step was to produce stereographic projections, then to show where the plates would intersect the sample surface assuming a $\{111\}_{\delta}$ habit plane. The stereographic projections were rotated until the trace lines were coincident with the plates observed in the micrograph. The matches for each grain are

very good, which tells us that the optical observations are consistent with a $\{111\}_\delta$ habit plane. However, there is no structural information leading us to choose the exact orientation of the stereographic projections. In order to make this more meaningful, we combined optical data with electron diffraction patterns recorded in the TEM.

A series of steps was used to examine the precipitate morphology of the macroscopic α' habit plane using TEM imaging and diffraction, optical microscopy, and computer simulations. A schematic diagram is shown in Figure 14 illustrating how this was achieved. First a TEM sample was made and electron diffraction patterns and images were taken near the edge of the sample with little or no tilt. Normally, we would choose an area that had a usable diffraction pattern without the need of tilting the sample. Once we recorded the diffraction pattern we would remove the sample from the microscope, find the area in a light microscope, then record an optical micrograph of the image. Next, we would determine the zone axis from the comparison with selected area diffraction simulations. With the zone axis known, we would produce a stereographic projection for that zone and create a trace analysis showing where the plates would intersect the sample surface given a $\{111\}_\delta$ and a $\{123\}_\delta$ habit plane. Finally, we would compare the traces of the stereographic projections to the plates in the optical micrograph.

One series of optical and TEM analyses of α' plates is shown in Figure 15. Here, a bright-field image is shown, which is on the $[\bar{4},1,3]_\delta$ zone axis, as determined by electron diffraction and simulation. There are also two stereographic projections for the $[\bar{4},1,3]_\delta$ zone axis, each with traces for the intersection of α' plates with a habit plane of $\{111\}_\delta$

and a $\{123\}_\delta$, respectively, with the sample surface. The two-phase Pu-Ga sample shows a large number of plates, and each set of plates, which corresponds to a trace, is given a color. Notice that the vast majority of the plates match the 4 variants for a plate with a $\{111\}_\delta$ habit plane; red, blue, brown, and green. The remaining plates can be accounted for by the traces for α' plates with a habit plane of $\{123\}_\delta$. After approximately 10 data sets, it was consistently found that 80% of the plates match the traces for a $\{111\}_\delta$ macroscopic habit plane. When considering this data, it must be observed that the $\{123\}_\delta$ orientation produces so many possible line traces that it becomes quite easy to fit the traces to experimental data. This is not the case for $\{111\}_\delta$, since there is only 4 possible traces. Therefore, it is a deficiency of this technique that given a few degrees of variation for each $\{123\}_\delta$ trace, there are not many orientations that can not be fitted. Another deficiency of this technique to keep in mind is that we are missing one variable of the precipitate orientation, namely the inclination relative to the normal of the plate face. These data further our understanding of the macroscopic habit plane, but do not yield a final answer, leaving us to consider further experiments. These future experiments that are need to solve the exact habit plane will be discussed at the end the manuscript.

It is possible that the two reported habit planes, $\{111\}_\delta$ and $\{123\}_\delta$, are each formed at one nose of the TTT diagram in Figure 6. Thus, if the two noses represent two distinct thermally activated mechanisms existing for this transformation, it may be that each nose produces a $\delta \rightarrow \alpha'$ martensitic transformation with a different habit plane. To date, there has been no clear evidence of this and the two-phase mixture created at both noses seem to have a mixture of plates. However, the noses are close enough that there is some

overlap of the two; meaning there may always be some mixture of the two transformations.

3.5. *Atomic structure of the α′/δ interface*

While the macroscopic habit plane has enough variation that converging on a final answer has proven difficult, the structure of the α′/δ interface at the atomic level has now been resolved. In this case, the interface is composed of a terrace and ledge structure which is faceted on $\{111\}_{\delta}$, as shown in the high-resolution TEM image in Figure 16. This means that the macroscopic interface and interfacial curvature is facilitated by the number and density of ledges at the interface.

Pond and Hirth [24,25] have proposed a topological model (TM) for addressing martensitic transformations rather than the phenomenological theory of martensitic transformation (PTMC) [26]. In their model, the transformation defects are first considered then used to predict a consistent habit plane and lattice orientation relationship directly from the geometry of the defects. A necessary result of their model is that there is a coherent terrace and ledge structure between the product and parent phases where transformation dislocations move in a diffusionless manner across the coherent terrace planes that separate the two phases. Our high-resolution TEM image in Figure 16 does indeed show that there is a terrace and ledge structure present at the α′/δ interface.

Hirth *et al.* [27] have applied the TM model directly to the $\delta \rightarrow \alpha'$ martensitic transformation and assumed that the step height at the α'/δ interface was twice the spacing of the close packed planes. Figure 16, however, exhibits steps which are considerably larger. Nonetheless, our high-resolution TEM images do answer the question asked by Hirth *et al.* [27]; does the terrace/dislocation model for the interface apply to the α'/δ interface given that the strains involved in the transformation are so large. To the best of our knowledge, Figure 16 presents the first known high-resolution TEM image of the α'/δ interface and does indeed support a terrace-ledge system with interface dislocations. The alternative they suggest, a nominally planar interface with large local disregistry that resembles a high-angle grain boundary or disclination, is simply not observed in our TEM results.

§4. FUTURE EXPERIMENTS

The data and interpretations presented here represent another step toward better understanding the physics and materials science of this fascinating transformation. Nonetheless, there is a considerable amount of work still to be done. Serial sectioning of a two-phase $\alpha' + \delta$ sample with structural information (diffraction) would be a logical step. However, we have two issues to overcome. First we do not have a scanning electron microscope with electron backscatter capability. Second, mechanical abrasion of the surface of these samples may cause the two-phase mixture of α' and δ to transform to α'. Therefore, we are working on a serial sectioning process that uses electropolishing and has a means to measure the depth of each polish. The later will be accomplished using

laser drilled holes and geometry. There is also a great need to do more experiments on the upper and lower nose of the TTT curve to better understand what the difference is between these transformations for both partially homogenized and fully homogenized samples. Finally, either dark-field or weak-beam TEM should to be done to examine the α'/δ interface and the density and configuration of dislocations present there.

§5. ACKNOWLEDGEMENTS

This work was performed under the auspices of the U.S. Department of Energy by University of California, Lawrence Livermore National Laboratory under Contract W-7405-Eng-48.

References:

1. S.S. Hecker, *Metall. Mater. Trans. A*, 35A, (2004) 2207-2222.
2. S.S. Hecker, "Plutonium and its Alloys" in Challenges in Plutonium Science, Vol. II, Los Alamos Science, Number 26, LANL, 2002. N.G. Cooper (Ed.) 290-335.
3. K. T. Moore, M. A. Wall, A. J. Schwartz, B. W. Chung, D. K. Shuh, R. K. Schulze, and J. G. Tobin, *Physical Review Letters*, 90 (2003), 196404.
4. G. van der Laan, K. T. Moore, J. G. Tobin, B. W. Chung, M. A. Wall, A. J. Schwartz, *Physical Review Letters*, 93 (2004), 097401.
5. P. Söderlind, *Advances in Phys.* 47 (1998), 959-998.
6. A.M Boring and J.L. Smith, "Plutonium Condensed Matter Physics" in Challenges in Plutonium Science, Vol. I, Los Alamos Science, Number 26, LANL, 2002. N.G. Cooper (Ed.) 90-127.
7. J. L. Smith and E. A. Kmetko, *J. Less Comm. Met.* 90 (1983), 83-88.
8. K.T. Moore, M.A. Wall, A.J. Schwartz, B.W. Chung, S.A. Morton, J.G. Tobin, S. Lazar, F.D. Tichelaar, H.W. Zandbergen, P. Söderlind, and G. van der Laan, *Philosophical Magazine*, 84 (2004), 1039-1056.
9. P. Söderlind and B. Sadigh, *Phys. Rev. Lett.* 92, (2004)185702.
10. S. S. Hecker and L. Fl Timofeeva, *Los Alamos Sci.* 26 (2000) 244.
11. J. T. Orme, M. E. Faiers, and B. J. Ward, in *Plutonium and Other Actinides*, edited by H. Blank and R. Lindner (North-Holland Publishing, Amsterdam, 1976), 761.
12. S.S. Hecker, D.R. Harbur, and T.G. Zocco, *Prog. Mat. Sci.*, 49 (2004), 429.
13. B.W. Leitch and S-Q Shi, 1996 *Modelling Simul. Mater. Sci. Eng.* **4** 281.

14. C.R. Krenn, M.A. Wall, and A. J. Schwartz, *MRS Proc.* 2004, 802, DD1.3.1-6.

15. C.R. Krenn, *Modelling Simul. Mater. Sci. Eng.* 12 (2004) 415.

16. M.A. Wall, A.J. Schwartz, M.J. Fluss, Sample Preparation for Transmission Electron Microscopy Characterization of Pu Alloys, UCRL-ID-141746.

17. T. G. Zocco, M. F. Stevens, P. H. Adler, R. I. Sheldon, and G. B. Olson, *Acta Metall. Mater.* 38 (1990)**,** 2275-2282.

18. K.J.M. Blobaum, C.R. Krenn, J.N. Mitchell, J.J., Haslam, M.A. Wall, T.B. Massalski, and A.J. Schwartz, "Evidence of transformation bursts during thermal cycling of a Pu-Ga alloy," *Metall. Mater. Trans. A*, In press.

19. J. N. Mitchell, M. Stan, D. S. Schwartz, and C. J. Boehlert, *Metall. Mater. Trans. A*, 35A, (2004) 2267-2278.

20. K.J.M. Blobaum, C.R. Krenn, M.A. Wall, T.B. Massalski, and A.J. Schwartz, "Nucleation and growth of the α' martensitic phase in Pu-Ga alloys," In preparation.

21. A. G. Crocker, *J. of Nuc. Mat.* 41, (1971),167-177.

22. Y. M. Jin, Y. U. Wang, A. G. Khachaturyan, C. R. Krenn, and A. J. Schwartz, *Metall. Mater. Trans. A*, 36A, (2005) 2031-2047.

23. P. H. Adler, G. B. Olson, and D. S. Margolies, *Acta Metall.* 34 (1986), 2053-2264.

24. R. C. Pond and J. P. Hirth, *Solid State Phys.* 47 (1994) 287.

25. J. P. Hirth and R. C. Pond, *Acta Mater.* 44 (1996) 4749.

26. M. S. Wechsler, D. S. Lieberman, and T.A. Read, *Trans AIME* 197 (1953) 1503.

27. J. P. Hirth, J. N. Mitchell, D. S. Schwart, and T. E. Mitchell, *Acta Metall.* In press.

Tables:

Table 1: The crystal structures, densities, and number of atoms per unit cell for the six solid allotropic phases of Pu and the liquid phase [2].

Phase	Crystal structure	Density (g/cm^3)	Atoms per unit cell
α	Monoclinic ($P2_1/c$)	19.86	16
β	Monoclinic ($C2/m$)	17.70	34
γ	Tetragonal ($Fddd$)	17.14	8
δ	Face-centered cubic $\left(Fm\bar{3}m\right)$	15.92	4
δ′	Tetragonal ($I4/mmm$)	16.00	4
ε	Body-centered cubic $\left(Im\bar{3}m\right)$	16.51	2
Liquid		16.65	

List of Figures:

Figure 1. The Wigner-Seitz radius of each metal as a function of *Z* for the 5*d*, 4*f*, and 5*f* metal series [after ref. 2].

Figure 2. A 'pseudo-phase' diagram of the phases present along the 5*f* actinide series [after ref. 6].

Figure 3. (a) A rearranged periodic table where the five transition metal series 4*f*, 5*f*, 3*d*, 4d, and 5*d* are shown [after refs. 6 and 7]. (b) A version of (a) where the number of solid allotropic phases for each metal is indicated by gray scale.

Figure 4. The atomic volume of all 6 phases of Pu as a function of temperature [2].

Figure 5. The Ga-rich side of the Pu-Ga binary phase diagram [10].

Figure 6. The time-temperature-transformation (TTT) diagram for a Pu alloy with 0.56 wt% Ga [11]. Contours show a given percentage of transformation from δ to α' as a function of time and temperature.

Figure 7. The continuous cooling dilatometry trace for a Pu-Ga alloy [2, 12].

Figure 8. (a) A plasmon TEM image acquired near a $\left[1\bar{1}0\right]_{\delta} \parallel \left[100\right]_{\alpha}$ zone axis showing an

α′ plate in δ matrix. The alternating twin slabs, which are discussed later in the text, are indicated. (b) A $\left[1\bar{1}0\right]_{\delta} \parallel \left[100\right]_{\alpha}$ diffraction pattern from a two-phase δ + α sample, where the reflections for each phase are indicated. Notice that while both phases are near a perfect orientation, each is a small degree off. (c) An atomic model that schematically shows the orientation relationship of α′ and δ at the atomic level.

Figure 9. (a) Elastic-plastic finite element calculation of the stress field (ranging from 250 MPa in tension to 850 MPa in compression) associated with a grown then reverted α′ plate in a δ-Pu matrix [14]. (b and c) two TEM images showing the background density of dislocations in δ-Pu and the density near the tip of an α′ plate, which differ by a factor of 6 to 7.

Figure 10. A series of bright- and dark-field TEM image of an α′ plate with multiple twin in a δ matrix. The corresponding diffraction pattern show the reflections for the two variants used for the dark-field TEM images.

Figure 11. A model of the α′ structure with periodically spaced twin boundaries. Assuming this structure, a diffraction pattern was calculated and compared to one acquired from a two-phase Pu sample, yielding a good match.

Figure 12. A figure showing the discrepancy between theory and our present experiments. On the left is an elastic phase-field simulation of the growth and

intersection of α′ plates in a single crystal of δ, producing 24 variants. On the right is a optical micrograph of α′ plates showing 4 variants [14].

Figure 13. An optical image of a two-phase mixture of α′ and δ [17]. In the image there are three grains, which are delineated by black lines. Three stereographic projections are also shown, each illustrating where a plate with a $\{111\}_\delta$ habit plane would intersect the sample surface [14].

Figure 14. A schematic diagram showing how we examine the precipitate morphology of the α' habit plane using TEM imaging and diffraction, optical microscopy, and computer simulations.

Figure 15. An optical micrograph of a two-phase sample with α' plates, which is near a $[\bar{4},1,3]$ zone axis. There are two stereographic projections for the $[\bar{4},1,3]$ zone axis, one showing where with α' plates would intersect the surface of the sample if they had a $\{111\}_\delta$ habit plane and one if they had a $\{123\}_\delta$ habit plane.

Figure 16. A high resolution TEM image of the α′/δ interface showing that the interface is composed of a number of terraces and ledges faceted on $\{111\}_\delta$.

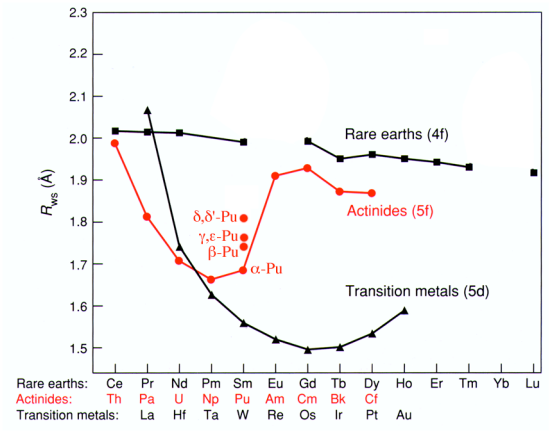

Figure 1

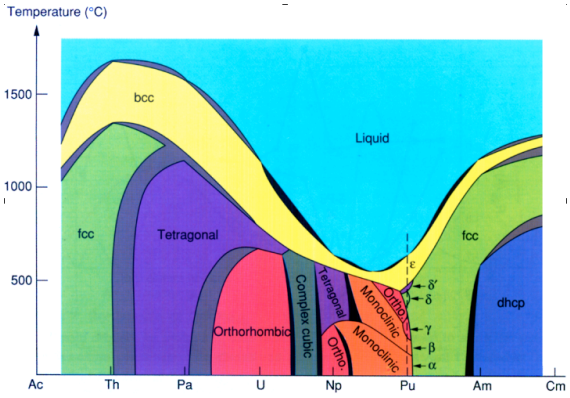

Figure 2

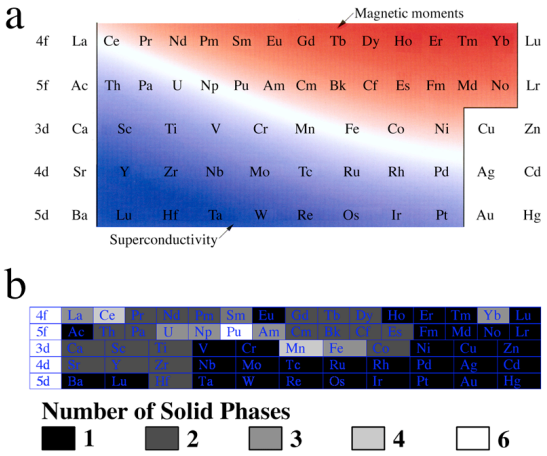

Figure 3

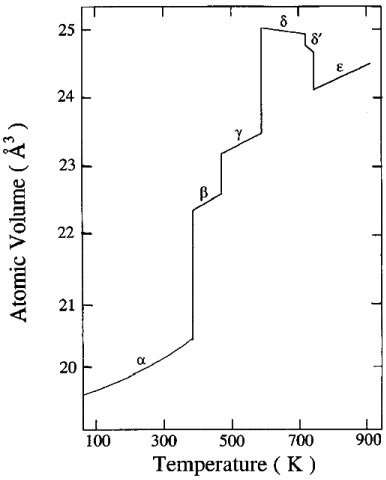

Figure 4

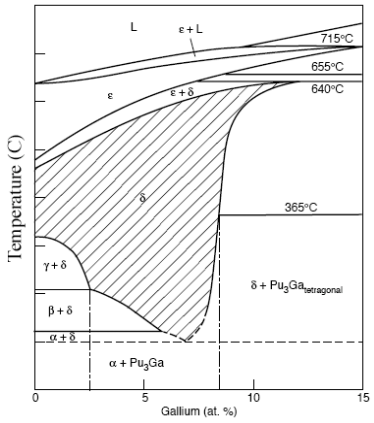

Figure 5

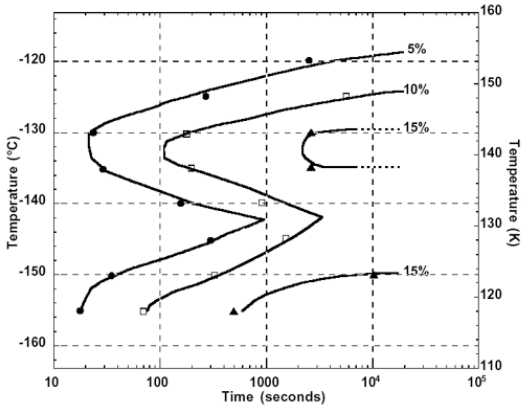

Figure 6

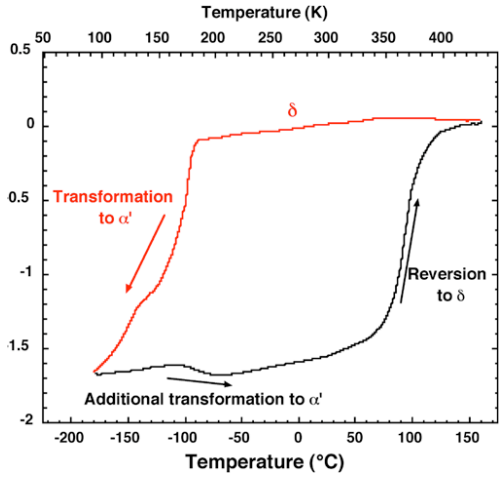

Figure 7

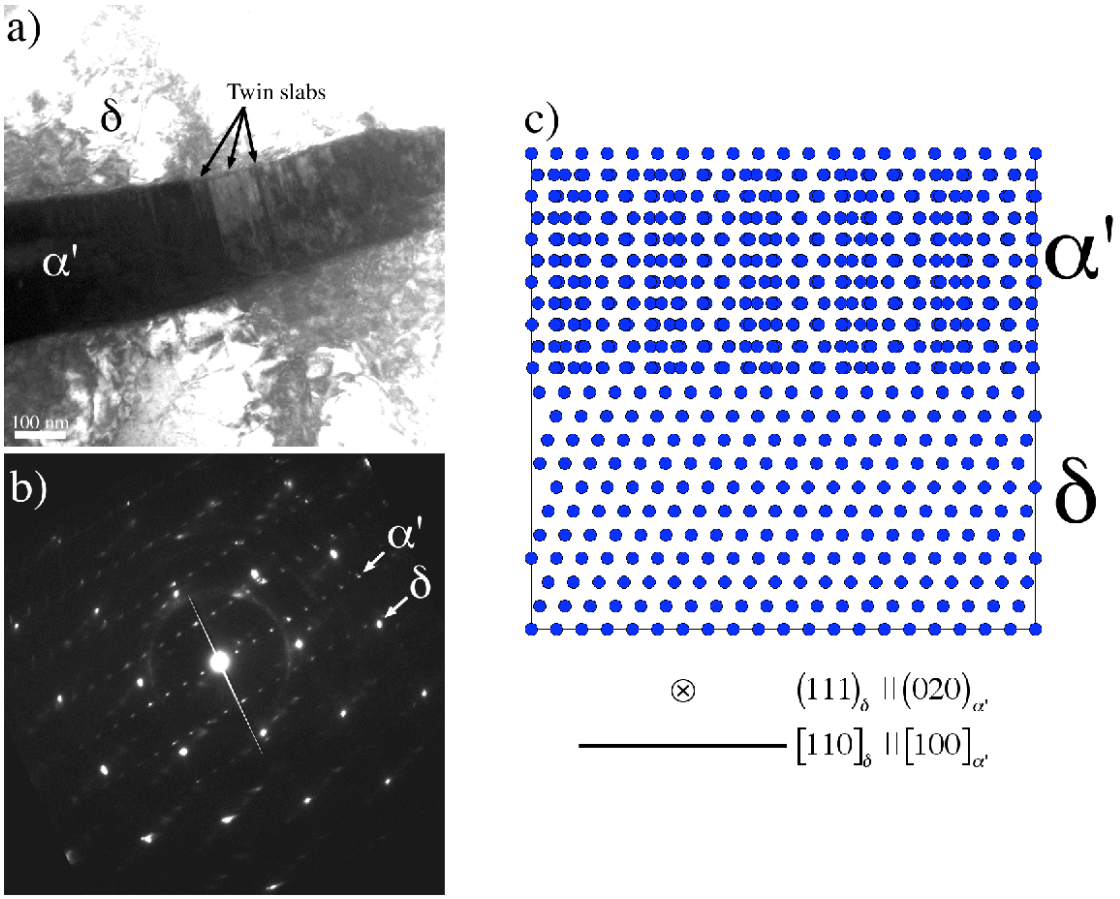

Figure 8

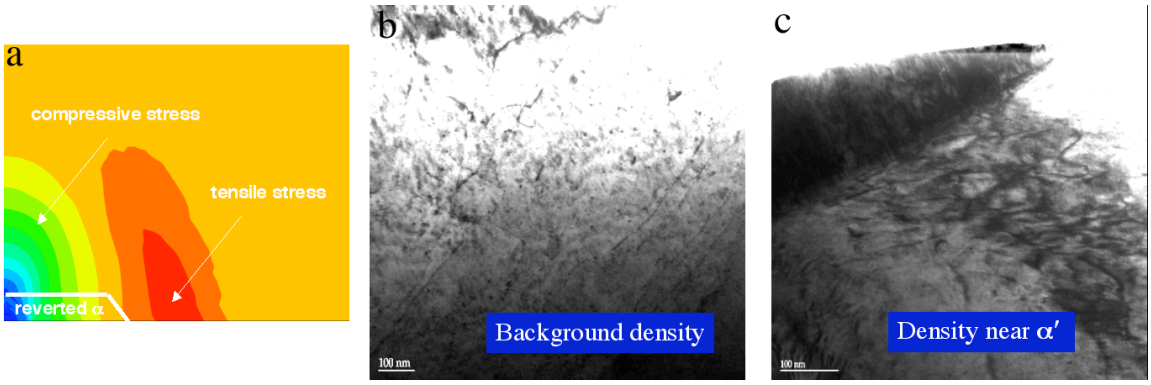

Figure 9

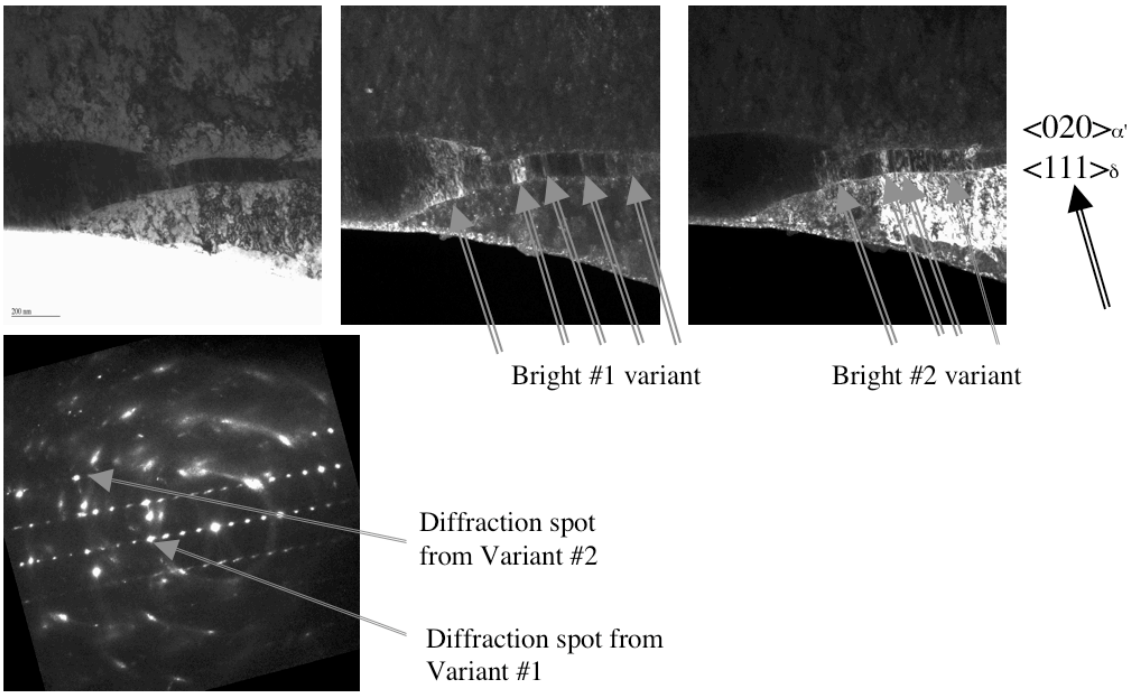

Figure 10

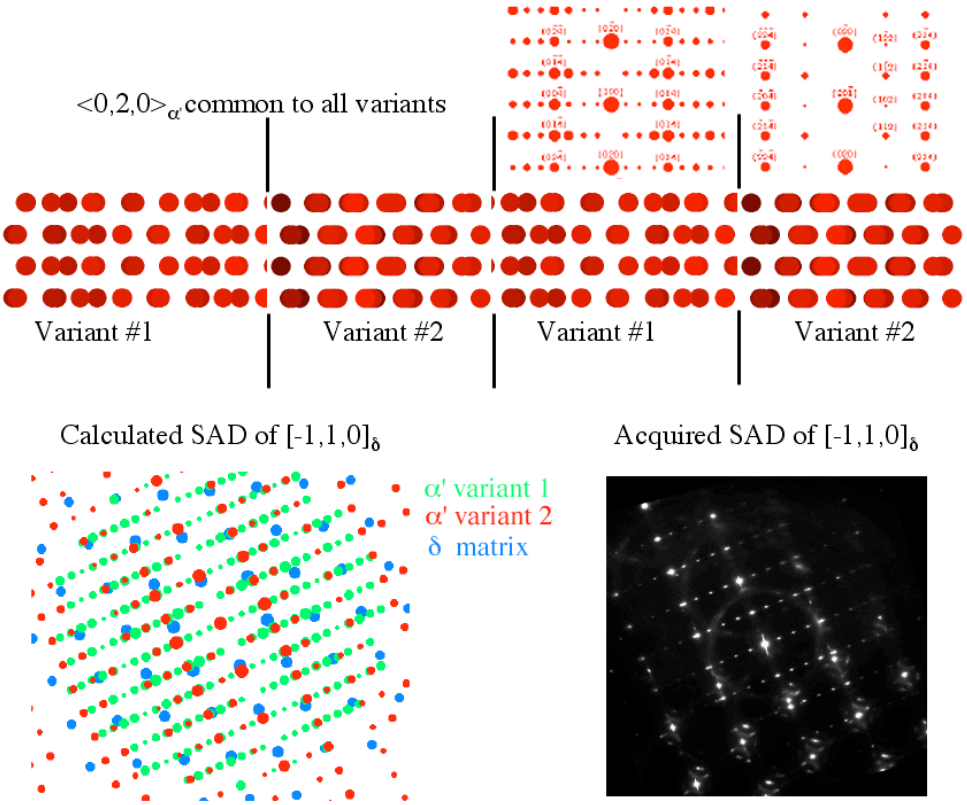

Figure 11

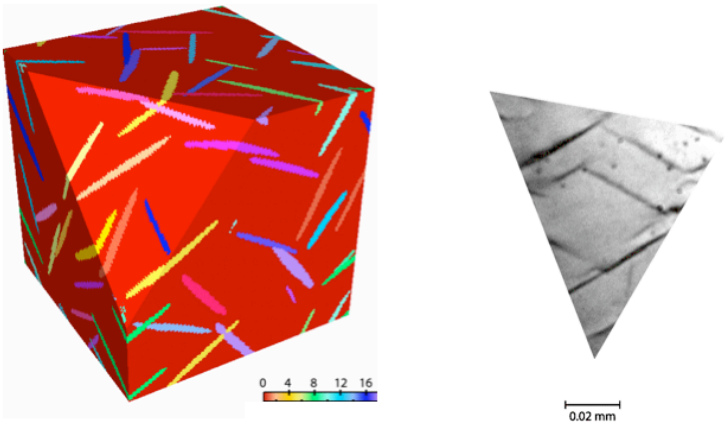

Figure 12

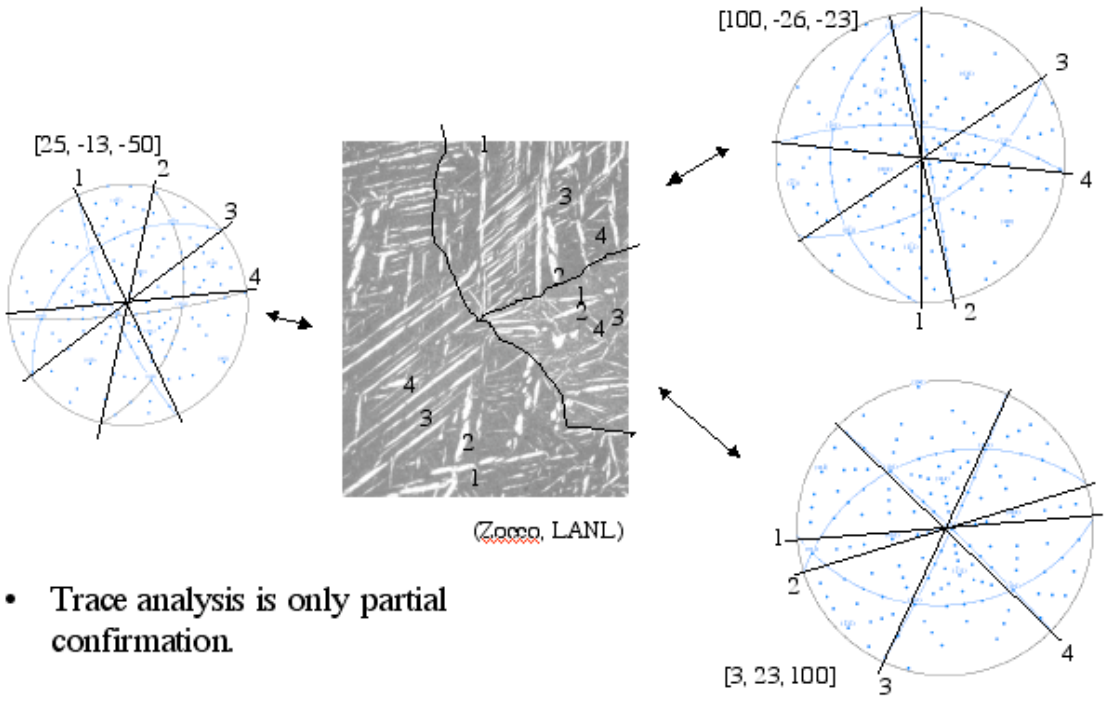

- Trace analysis is only partial confirmation.

Figure 13

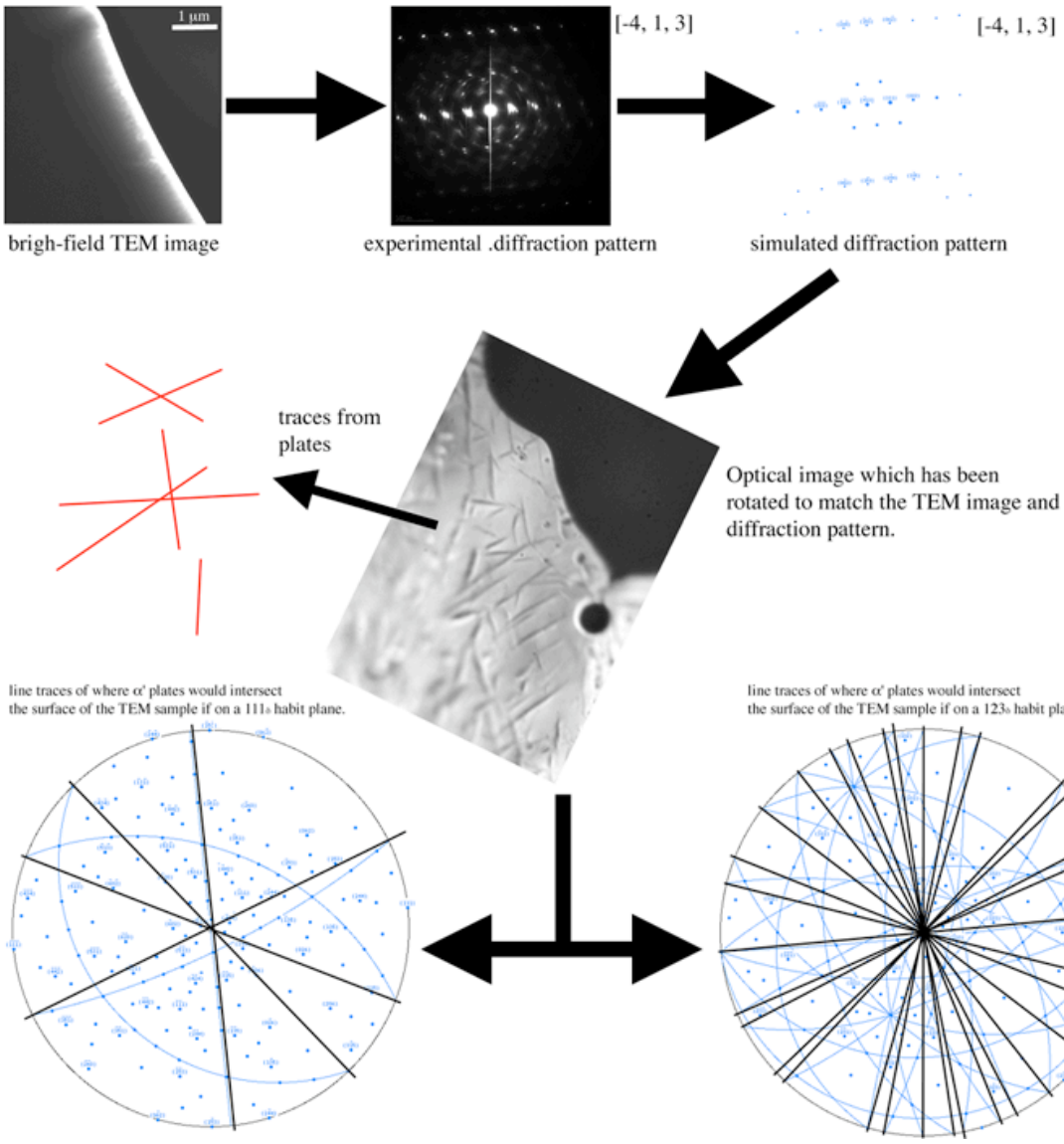
1 μm
[-4, 1, 3]
[-4, 1, 3]
brigh-field TEM image
experimental .diffraction pattern
simulated diffraction pattern
traces from plates
Optical image which has been rotated to match the TEM image and diffraction pattern.
line traces of where α' plates would intersect the surface of the TEM sample if on a 111b habit plane.
line traces of where α' plates would intersect the surface of the TEM sample if on a 123b habit plane.

Figure 14

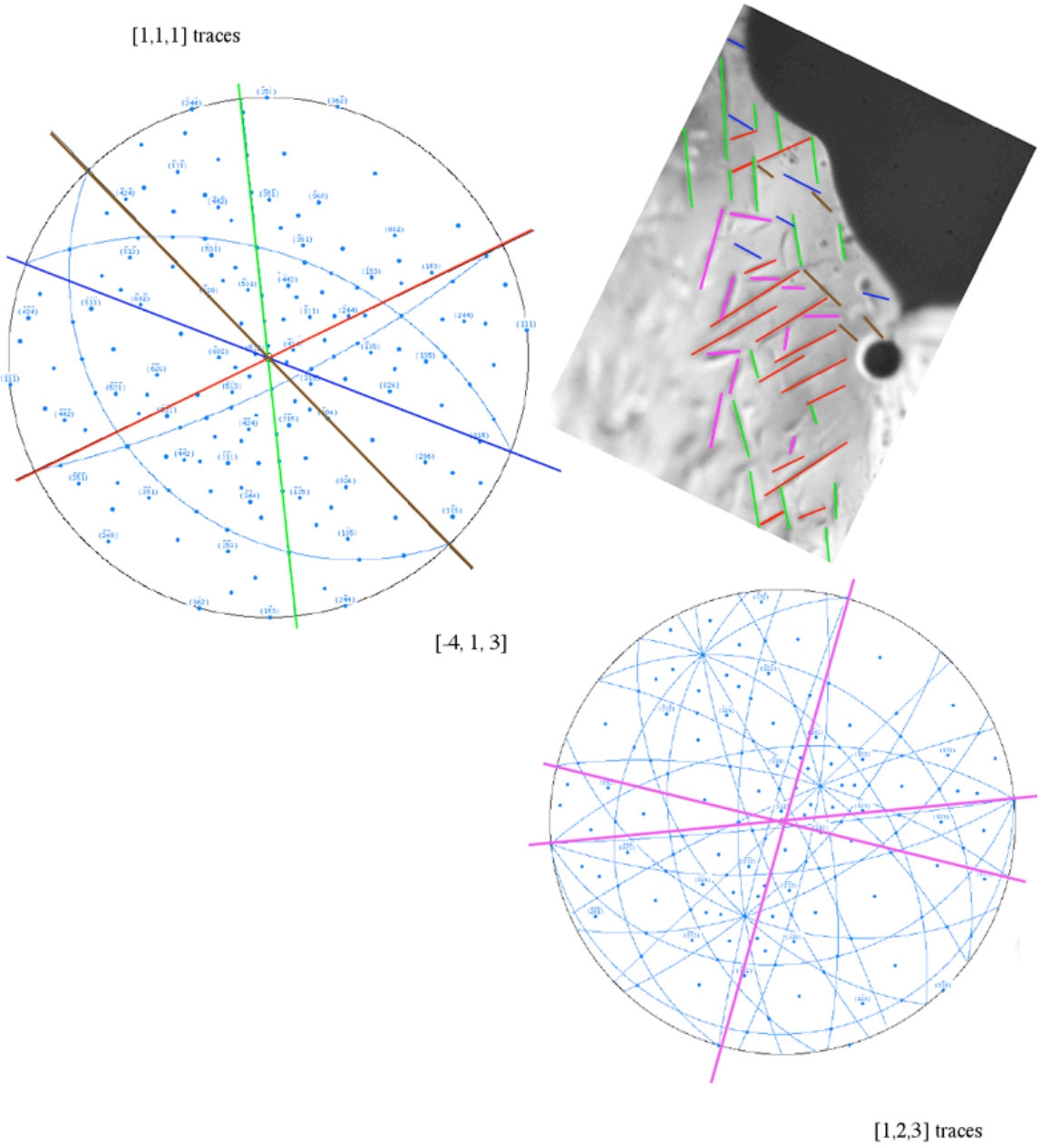

Figure 15

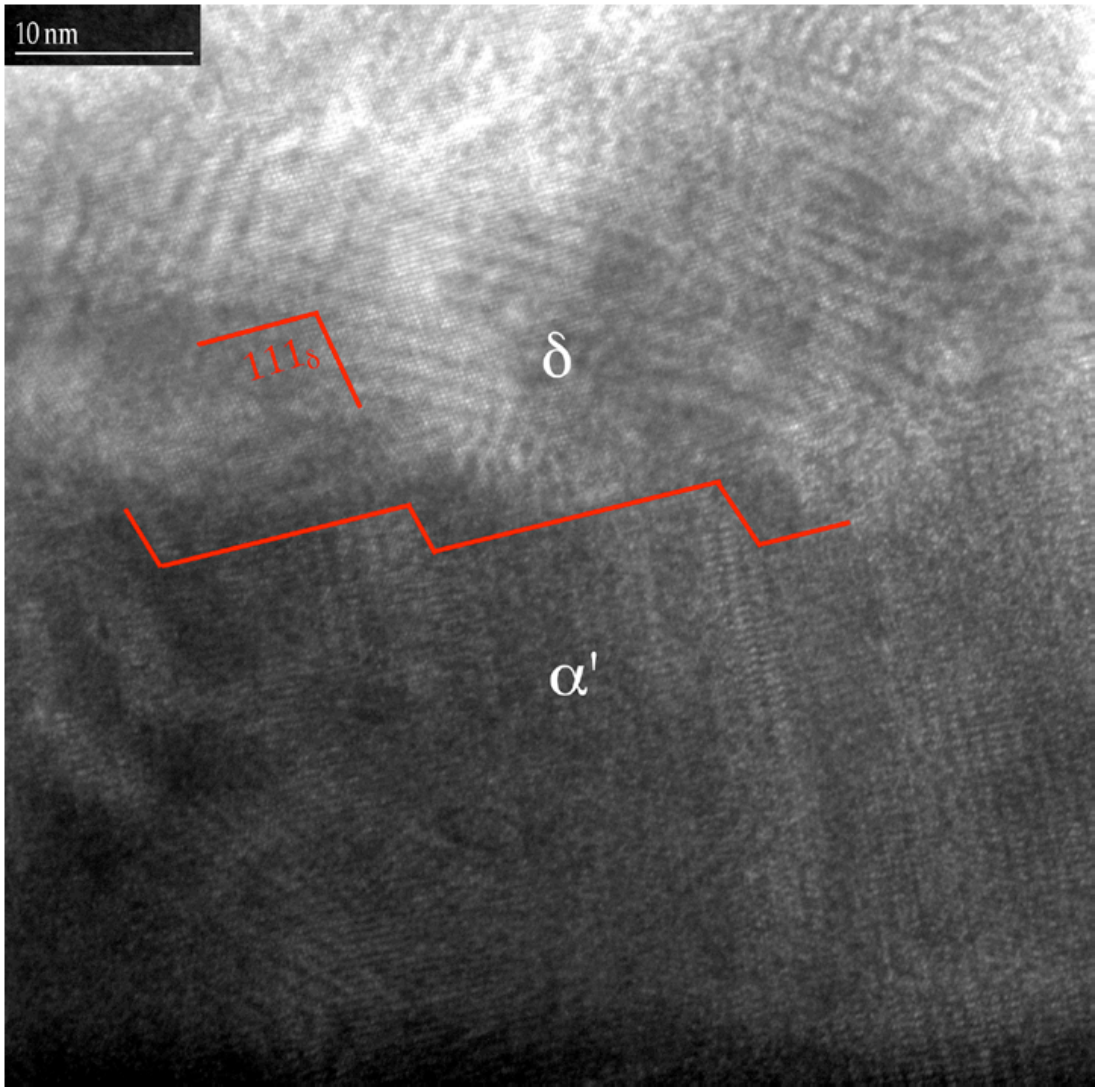

Figure 16